Modeling the Effect of Air-Gap Length and Number of Turns on Ferrite-Core Inductors Working up to Magnetic Saturation in a Buck Converter

Alessandro Ravera, *Student Member, IEEE*, Andrea Formentini, *Member, IEEE*, Matteo Lodi, *Member, IEEE*, Alberto Oliveri, *Member, IEEE*, Massimiliano Passalacqua, *Member, IEEE*, and Marco Storace, *Senior Member, IEEE*

***Abstract*— In this work, a nonlinear behavioral circuit model is proposed for air-gapped ferrite-core inductors working up to magnetic saturation. The model comprises a nonlinear conservative inductor, with current-dependent inductance, and two linear resistors, accounting for losses in both the winding and the core. Two representations are proposed for the nonlinear inductance, parameterized by both the number of turns and the air-gap length. The model (in both versions) is identified and validated through experimental measurements collected on a real buck converter. Inductor voltages and currents are used for parameter identification. The obtained results exhibit a good match with the experimental measurements used for validation purposes. An example of the application of the model to the design of a buck converter exploiting partially saturating inductors is also proposed.**

***Index Terms*— Power inductor, magnetic saturation, gapped ferrite core, nonlinear circuit model.**

I. Introduction

SWITCH mode power supplies (SMPSs) are typically equipped with ferrite-core inductors [1], [2], which often constitute the largest and bulkiest components in the converters. Therefore, the increasing demand for a higher power density, especially for automotive and aerospace applications, requires also smaller (and lighter) inductors. However, for a given inductance value, the smaller the magnetic core volume, the higher the number of necessary turns, and then the magnetization of the core. This leads the inductor to approach magnetic saturation for smaller current values. A drawback of ferrite cores is that their permeability - related to the inductance - quickly drops when the applied magnetic field exceeds a threshold value [3]. To mitigate this effect, an air gap is often inserted in the core, which decreases the overall permeability, thus allowing the inductor to operate in its linear region for a wider current range [4]. In commercial inductors, the gap length is fixed by the manufacturer, whereas in custom components it can be regulated *ad hoc*, together with the number of turns, to achieve the desired inductance and linearity range. Usually, the air-gap length is very small, compared to the overall core length, since a wider gap leads to the so-called *fringing effect* [5]: the magnetic field lines inside the gap are not straight, but leak far into the neighboring areas, possibly intersecting the windings and causing eddy current losses. This issue can be alleviated by resorting to distributed air gaps [6], also obtained through iron-powder cores [7]. Owing to the air gap, it is possible to reduce the core size of inductors still working in their linear region.

An even higher size reduction could be obtained by using gapped inductors working in partial magnetic saturation. Recent works investigate how to exploit saturation to sensibly increase the power density and, in some cases, also the efficiency of DC-DC converters [8], [9], [10], [11], [12], [13], [14] and inverters [15], [16], [17], [18]. A survey on the application of saturating inductors in power supplies is given in [19].

Magnetic components can be studied through field simulations, possibly resorting to finite-element analysis, where the electric and magnetic fields are computed as a function of time and space. Inductance, power losses, and other modeling elements can be obtained from these simulations as aggregate information. In this framework, several models of saturating ferrite-core inductors with air gap have been proposed [4], [20], [21]. These techniques require the knowledge of some geometric and magnetic properties of the component, which are often undisclosed for commercial inductors.

As an alternative, circuit (behavioral) models can be obtained, where the component is characterized by relying only on voltage-current measurements at its terminals. These models are more suitable to be embedded within circuit simulators to design, numerically emulate, and control circuits containing magnetic components, such as power converters. Several behavioral models of ferrite-core inductors working up to partial magnetic saturation are available in the literature [19], [22], [23], [24], [25], [26], [27], [28], [29], [30], [31]. The inductor power losses are also modeled, with different approaches. However, to the best of the authors' knowledge, no behavioral models are available that account for the

Manuscript received 2 April 2024; revised 7 June 2024; accepted 18 June 2024. This work was supported in part by European Union—NextGenerationEU, within the Project "Exploiting MAGnetic SATuration (MAGSAT) to Increase Power Density in Switching Converters," University of Genoa, Italy. This article was recommended by Associate Editor J. Anders.
(Corresponding author: Alberto Oliveri.)

The authors are with the Department of Electrical, Electronic, Telecommunications Engineering and Naval Architecture, University of Genoa, 16145 Genoa, Italy (e-mail: alberto.oliveri@unige.it).
Color versions of one or more figures in this article are available at https://doi.org/10.1109/TCSI.2024.3421261.

Digital Object Identifier 10.1109/TCSI.2024.3421261

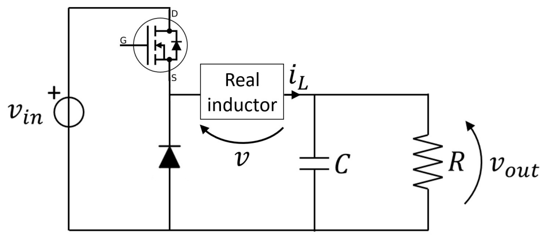

Fig. 1. Circuit schematic of the buck converter.

inductance and power loss up to magnetic saturation and are parameterized by the number of turns and air-gap length. The main novelty of this work is a behavioral nonlinear circuit model (in two variants) that accounts for both the air-gap length and the number of turns. The model is validated for different operating frequencies, thus substantially generalizing the preliminary analysis proposed in [32].

In both versions (called *model 1* and *model 2*), the model parameters are identified starting from a limited set of voltage and current measurements obtained on a buck converter, where the inductor voltage turns out to be a square wave with a specific period, amplitude, and duty cycle. The circuit model is composed of a nonlinear conservative inductor and two linear resistors, that capture the power losses of the real inductor. The two variants differ in how the nonlinear inductance of the conservative inductor is modeled: model 1 is mainly based on a physical approach and requires the knowledge of some geometrical parameters such as the core section area and mean magnetic path length; model 2 is derived from model 1, but is based on a black-box approach [33], where no geometrical features are required. The obtained results show a good matching with the experimental measurements, even those not used for training purposes, for different air-gap values, number of turns, and SMPS operating conditions.

The proposed models can be easily included in circuit simulators and can be an effective tool to design, numerically emulate, and control high-power-density SMPSs exploiting air-gapped ferrite-core inductors working up to partial saturation. An example of how these models can be used for SMPS design purposes is included.

The paper is organized as follows: Sec. II describes the adopted experimental setup, Sec. III details the two proposed models. The obtained results are shown in Sec. IV, before drawing some conclusions in Sec. V.

II. Experimental Setup

In this work, we consider a real buck converter, whose circuit schematic is shown in Fig. 1, which comprises a metal-oxide-semiconductor field-effect transistor (MOSFET), a diode, an output LC filter, and a resistive load. The MOSFET is controlled using a pulse width modulation (PWM) technique, producing a square wave signal with period T and duty cycle $D \in [0, 1]$. In ideal conditions (no losses), the average steady-state converter's output voltage is $v_{out} = Dv_{in}$. In real conditions, the average output voltage will be lower, due to power losses on both the semiconductor devices and the passive components (mainly the inductor).

Two IRF250P225 MOSFETs (by Infineon) are used to implement the converter leg shown in Fig. 1. The control signals are sent from a dSpace control platform to the converter

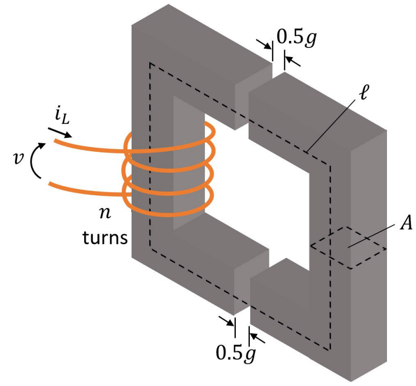

Fig. 2. Magnetic core with an air gap.

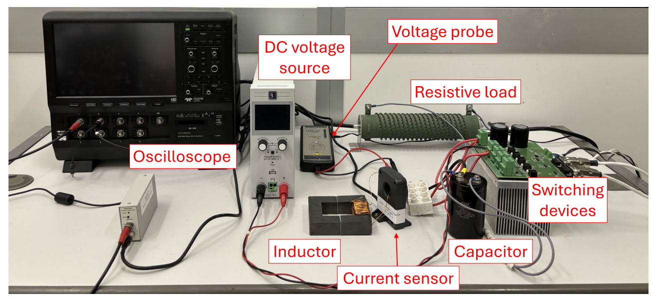

Fig. 3. Experimental setup.

through optical fibers. The output capacitor and resistor have capacitance $C = 40\,\mu\text{F}$ and resistance $R = 4.5\,\Omega$, respectively. The inductor is composed of two U-shaped ferrite-cores (P-material) OP-49925-UC [34] (see Fig. 2), combined to form a ring of dimensions $101.6\,\text{mm} \times 114.2\,\text{mm}$. The mean magnetic path length is $\ell = 308\,\text{mm}$ and the section area is $A = 645\,\text{mm}^2$. To create the inductor, a copper wire of 1 mm in diameter and 3.5 m in length is wound around one side of the core, by creating a winding with n turns. An air gap of length $g \ll \ell$ is obtained by inserting several sheets of paper between the two halves of the core, on both sides. The experimental setup is shown in Fig. 3.

The parameters of the proposed circuit models are identified only based on steady-state measurements of the inductor voltage v and current i_L, obtained with $n = \{20, 25, 30\}$ and $g = \{0.2, 0.4, 0.6, 0.8, 1\}$ mm.[1] The data are measured using a Hioki CT6862-05 AC/DC current sensor and a Pico Technology 100 MHz differential voltage probe connected to a 500 MHz, 12-bit Lecroy MDA805A oscilloscope. This setup ensures proper acquisition accuracy. For each combination of n and g, the inductor is connected to the buck converter and three different PWM frequencies are applied: $f = \{20, 35, 50\}$ kHz. For each of them, the input voltage v_{in} and the PWM duty cycle D are changed within ranges $[10, 100]$ V and $[0.5, 0.7]$, respectively, thus obtaining 7 different operating conditions characterized by different current biases and amplitudes, spanning from the linear region to the partial magnetic saturation. Therefore, a total of 147 datasets $\left\{\hat{v}^{(k)}(t_j), \hat{\imath}_L^{(k)}(t_j)\right\}$ is available, with $k = 1, \ldots, 147$, $j = 1, \ldots, N_s^{(k)}$, where $N_s^{(k)}$ is the number of samples in the k-th dataset and $t_j = (j-1)T_s$, with sampling time $T_s = 20\,\text{ns}$. As an example, Fig. 4 shows

[1] For $n = 20$ and 25, used for model validation, we collected measurements only for $g = 0.4$ mm.

This article has been accepted for inclusion in a future issue of this journal. Content is final as presented, with the exception of pagination.

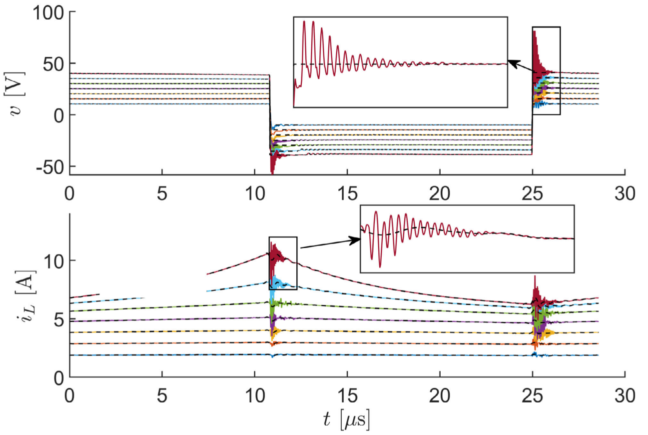

Fig. 4. Measurements of inductor voltages (top panels) and currents (bottom panels) with $n = 30$, $g = 0.4$ mm, and $f = 35$ kHz. Raw (colored curves) and filtered (black dashed curves) data. The insets show voltage and current for an interval of 1.5 µs after switching.

the 7 inductor voltages (top panel) and currents (bottom panel) obtained for $n = 30$, $g = 0.4$ mm, and $f = 35$ kHz. For small current values, the inductor works in its linear region; as the current increases, the inductor approaches magnetic saturation, which causes the typical cusp-like shapes, visible in the higher curves in the bottom panel. Notice that the current has a DC bias and significant high-frequency oscillations occur for about 1.5 µs after the switching times, both on the voltage and current measurements (see the insets in the figure). Since these oscillations would affect the model identification, voltages and currents are filtered, thus obtaining the dashed curves in the figure. The maximum measured converter output power was about 1 kW. For the k-th dataset, the instantaneous and average power are evaluated as $\hat{p}^{(k)}(t_j) = \hat{v}^{(k)}(t_j)\,\hat{\imath}_L^{(k)}(t_j)$ and $\langle \hat{p}^{(k)} \rangle = \frac{1}{N_s^{(k)}} \sum_{j=1}^{N_s^{(k)}} \hat{p}^{(k)}(t_j)$.

In all cases, due to the large size of the inductor core, we did not experience any current thermal drift, even when the inductor operated in saturation for a long time. Therefore, the temperature is not considered in this work, and the proposed models are valid only when the effects of the temperature are negligible.

III. Nonlinear Model of the Ferrite-Core Inductor

Typical B-H loops at 25°C and 100°C of the P-material composing the ferrite core are shown in Fig. 5, with gray and black solid lines, respectively.

A. Linear Region

For low values of B and H, the material can be assumed to be linear. In these conditions, we consider sinusoidal fields $B(t) = A_B \cos(\omega t + \theta_B)$ and $H(t) = A_H \cos(\omega t + \theta_H)$, with angular frequency ω, amplitudes A_B and A_H and phase θ_B and θ_H, respectively. Their corresponding phasors are defined as $\dot{B} = A_B e^{j\theta_B}$ and $\dot{H} = A_H e^{j\theta_H}$, whereas the complex permeability is [35], [36]

$$\begin{aligned}\mu &= \frac{\dot{B}}{\dot{H}} = \frac{A_B}{A_H} e^{-j(\theta_H - \theta_B)} \\ &= \frac{A_B}{A_H}\cos(\theta_H - \theta_B) - j\frac{A_B}{A_H}\sin(\theta_H - \theta_B) \triangleq \mu' - j\mu''. \quad (1)\end{aligned}$$

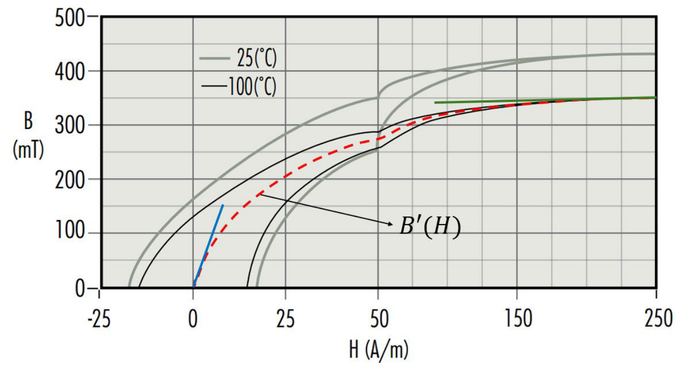

Fig. 5. Typical B-H loop of the P-material at two different frequencies. The red dashed curve is the component B', whereas the blue and green segments evidence the slopes of the curve for small and large values of H, respectively.

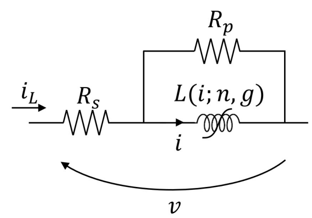

Fig. 6. Equivalent circuit model of the ferrite-core inductor.

The complex relative permeability is $\mu_r = \frac{\mu}{\mu_0} = \frac{\mu'}{\mu_0} - j\frac{\mu''}{\mu_0} = \mu_r' - j\mu_r''$, where μ_0 is the vacuum permeability. Therefore,

$$\dot{B} = \mu_0(\mu_r' - j\mu_r'')\dot{H} = \mu_0\mu_r'\dot{H} - j\mu_0\mu_r''\dot{H} \triangleq \dot{B}' + j\dot{B}''. \quad (2)$$

Phasor $\dot{B}'$ is in phase with $\dot{H}$, whereas $\dot{B}''$ has a phase shift due to losses. In the time domain, this means that $B(t)$ is the sum of a term $B'(t)$ proportional to $H(t)$ and a term $B''(t)$, related to $H(t)$ through a differential equation, leading to a phase shift. The magnetic flux across the core section (of area A) can also be written as $\phi(t) = A[B'(t) + B''(t)] \triangleq \phi'(t) + \phi''(t)$, by assuming field B to be uniform.

B. Nonlinear Region

In the linear region we have $B'(t) = \mu_0\mu_r' H(t)$. By increasing H, the relationship between B' and H, shown as a dashed red curve in Fig. 5 for the case at 100°C, becomes nonlinear. We define the *differential permeability* $\mu_d(H) = \frac{1}{\mu_0}\frac{dB'}{dH}$, i.e., the slope of this curve.[2] For low values of H, $\mu_d = \mu_d^0$, in the order of magnitude of 10^3, for the considered core (blue segment in Fig. 5). The differential permeability drops to about 1 in deep saturation (green segment in Fig. 5). We model the ferrite-core inductor with the circuit shown in Fig. 6 [32]. The model is composed of a conservative nonlinear inductor with current i and nonlinear differential inductance $L(i; n, g)$ (parameterized by the number of turns n and the air-gap length g) and two linear resistors with resistance R_s and R_p. As the magnetic flux ϕ' is proportional to B' and the inductor current i depends on H, the differential inductance $L(i; n, g) = \frac{d(n\phi')}{di}$ is related to the differential permeability μ_d. The classical conservative inductor model with constant inductance allows reproducing only the linear B'-H behavior (blue segment in Fig. 5). This is clearly

[2] Notice that, in the linear region, the differential permeability coincides with the relative permeability.

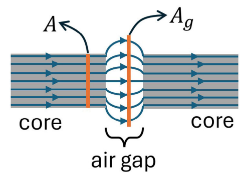

Fig. 7. Frontal section of a portion of the core with the air gap. The field lines of the flux density B are shown in blue.

inadequate when the inductor works in partial saturation. The nonlinear conservative inductor allows reproducing the flux ϕ' (corresponding to B'), whereas the resistors model both winding and core losses, thus leading to the whole flux $\phi = \phi' + \phi''$, also including the winding losses. In particular, R_s is the DC resistance of the windings and R_p accounts for the magnetic losses, causing part of the current i_L not to contribute to the generation of flux in the inductor. In addition, the presence of the resistance R_p causes the losses of the circuit to vary with the frequency of the applied voltage v. By considering v and i_L as the descriptive variables, the model equations are

$$\begin{cases} \dfrac{di}{dt} = -\dfrac{R_s R_p}{L(i;n,g)(R_s+R_p)} i + \dfrac{R_p}{L(i;n,g)(R_s+R_p)} v \\ i_L = \dfrac{R_p}{R_s+R_p} i + \dfrac{1}{R_s+R_p} v. \end{cases} \tag{3}$$

This model allows obtaining numerically the inductor current i_L for any assigned v, for different values of n and g.

Two different models are proposed, for the nonlinear inductance $L(i;n,g)$, described in the following subsections.

C. Model 1 (Physics-Based)

Let H_g, B'_g, and ϕ'_g be the magnetic field strength, flux density, and magnetic flux inside the air gap.

Due to the fringing effect, the magnetic field tends to bend outside, in the air gap region (see Fig. 7), by crossing a surface of area $A_g > A$. A practical rule to model this effect, suggested in [37] for $g \ll \ell$ and $g^2 \ll A$, is to consider $A_g = (1+\alpha g)A$, being α a positive tuning parameter that can be related to the physical dimensions of the core. According to Gauss's law, the magnetic flux crossing the surface (with area A) inside the core is equal to the magnetic flux crossing the surface (with area A_g) inside the gap, i.e., $\phi' = \phi'_g$. This leads to $B'A = B'_g A_g$ and $B'_g = B' \frac{A}{A_g} = \frac{B'}{(1+\alpha g)}$. Therefore, when the inductor works in its linear region, $H = \frac{B'}{\mu_d^0 \mu_0}$ and $H_g = \frac{B'_g}{\mu_0} = \frac{B'}{(1+\alpha g)\mu_0}$. According to Ampere's law (Ch. 4 of [35]), it follows that

$$i(B';n,g) = \frac{1}{n}\left[H(B')\ell + H_g(B')g\right] = \tag{4}$$

$$= \frac{1}{n}\left[\frac{B'}{\mu_d^0 \mu_0}\ell + \frac{B'}{(1+\alpha g)\mu_0} g\right]. \tag{5}$$

We define an equivalent gap

$$\tilde{g}(g) = \frac{g}{1+\alpha g} < g. \tag{6}$$

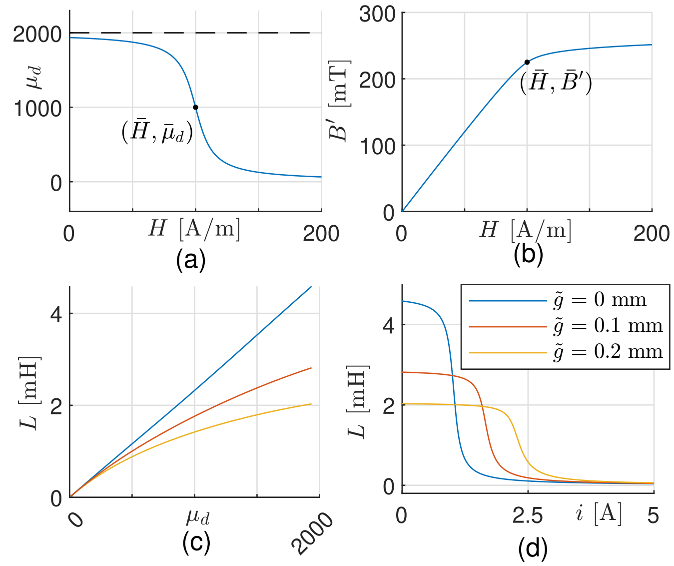

Fig. 8. Parameter setting: $\xi_1^{(1)} = 2000$, $\xi_2^{(1)} = 1$, $\xi_3^{(1)} = 10$, $\xi_4^{(1)} = 100\mathrm{Am}^{-1}$, and $n = 30$. (a) Differential permeability μ_d vs magnetic field H; (b) B' vs H; (c) $L(i;n,g)$ vs μ_d, for and $\tilde{g} = 0$ mm (blue), $\tilde{g} = 0.1$ mm (orange), and $\tilde{g} = 0.2$ mm (yellow); (d) $L(i;n,g)$ vs i, for the same gap values.

An experimental validation of the Eq. (6) is provided in Appendix A. The differential inductance is defined as

$$L(i;n,g) = \frac{d(n\phi')}{di} = \frac{n^2 A\, dB'}{\frac{dB'}{\mu_d^0 \mu_0}\ell + \frac{dB'}{\mu_0}\tilde{g}} = \frac{n^2 A \mu_0 \mu_d^0}{\ell + \tilde{g}\mu_d^0}. \tag{7}$$

We want to generalize this formulation to include magnetic saturation. Let us first define the function

$$\gamma(z;\xi) = \xi_2 + \frac{\xi_1 - \xi_2}{2}\left\{1 - \frac{2}{\pi}\arctan\left[\xi_3\left(\frac{|z|}{\xi_4} - 1\right)\right]\right\} \tag{8}$$

where $\xi = [\xi_1, \xi_2, \xi_3, \xi_4]$, $\xi_1, \ldots, \xi_4 > 0$, $\xi_1 > \xi_2$. This function assumes the values ξ_1, ξ_2, and $\frac{\xi_1+\xi_2}{2}$ for $|z| \ll \xi_4$, $|z| \gg \xi_4$, and $|z| = \xi_4$, respectively. Moreover, ξ_3 controls the slope of the curve for $|z| = \xi_4$, being $\left.\frac{d\gamma}{dz}\right|_{|z|=\xi_4} = -\frac{(\xi_1-\xi_2)\xi_3}{\pi\xi_4}$.

In this first modeling approach, we consider $\mu_d(H) = \gamma(H;\xi^{(1)})$, where $\xi^{(1)}$ denotes the parameter vector for model 1. Since, due to saturation, $\mu_d \approxeq 1$ for large values of H, we fix $\xi_2^{(1)} = 1$. A curve $\mu_d(H)$ for a given parameter set (see figure caption) is shown in Fig. 8 (a). Without the air gap, the differential inductance $L(i;n,g)$ is proportional to μ_d, therefore this model comes down to the one proposed in [38] and exploited in many other works [22]. In the presence of an air gap, however, the differential inductance assumes a different shape, depending on both n and g.

The magnetic induction B' can be obtained as

$$B'(H) = \int_0^H \mu_0 \mu_d(h)\, dh \tag{9}$$

where the integral can be computed either analytically, even if the resulting expression is quite long, or numerically. In any case, we can obtain a look-up table (LUT) with a vector of samples of H and the corresponding values of B'; in this work we use 1000 points. As shown in Fig. 8 (b), the function $B'(H)$ is bijective. Therefore, its inverse $H(B')$ does exist and can be evaluated through the available LUT. Equation (5) can be recast, in the nonlinear region, as

$$i(B'; n, g) = \frac{1}{n}\left[H(B')\ell + \frac{B'}{\mu_0}\tilde{g}\right]. \tag{10}$$

The current i is a bijective function of B', parameterized by n and g. Its inverse $B'(i; n, g)$ can be obtained through the LUT, for different values of n and g. The differential inductance (see Eq. (7)) can be recast as

$$L(i; n, g) = \frac{n^2 A\, dB'}{\frac{dH}{dB'}dB'\ell + \frac{dB'}{\mu_0}\tilde{g}} = \frac{n^2 A\mu_0\mu_d(H)}{\ell + \tilde{g}\mu_d(H)}. \tag{11}$$

L depends nonlinearly on μ_d (for $g > 0$), as shown in Fig. 8 (c) and μ_d depends in turn on H, and therefore on i, n, and g. The curves $L(i; n, g)$ are shown in panel (d) for different values of g.

By summarizing, model 1 depends on 4 parameters, namely $\xi_1^{(1)}$, $\xi_3^{(1)}$, $\xi_4^{(1)}$, and α, and assumes that the magnetic path length ℓ and core section area A are known.

D. Model 2 (Black-Box)

By looking at the plots in Fig. 8 (d), we can approximate these curves through the function γ defined in Eq. (8). Therefore, with model 2, we assume:

$$L(i; n, g) = \gamma(i; \xi^{(2)}(n, \tilde{g})) \tag{12}$$

where $\xi_1^{(2)}$ (i.e., the inductance for small currents) decreases with g, and $\xi_4^{(2)}$ (i.e., the value of i such that the inductance is about one half of the nominal inductance) increases with g. More precisely, we consider:

$$\xi_1^{(2)}(n, g) = \frac{n^2}{c_1\tilde{g} + c_2} \tag{13}$$

$$\xi_2^{(2)}(n) = \frac{n^2}{c_3} \tag{14}$$

$$\xi_4^{(2)}(n, g) = \frac{c_4\tilde{g} + c_5}{n} \tag{15}$$

Parameter $\xi_3^{(2)}$ does not depend on n and g. The derivation of these expressions is detailed in Appendix B. Model 2 depends on 7 parameters: $c_1, \ldots, c_5$, $\xi_3^{(2)}$, and α. Different from model 1, which is mainly based on the physics of the inductor and requires the knowledge of some geometrical parameters, model 2 is completely behavioral and none of its coefficients has a direct physical meaning.

IV. Results

A. Model Identification

The whole inductor model contains the 4 (7) parameters of model 1 (model 2) and the resistances R_s, R_p. All these 6 (9) model parameters are collected in a vector x and the differential inductance can be expressed as a function $L(i; n, g, x)$. The model behavior can vary with the frequency due to its structure.

The optimal vector x^* is identified by exploiting a subset $\mathcal{K}$ of the experimental measurements described in Sec. II, with sampling time T_s, and solving the following nonlinear optimization problem,

$$\min_x \frac{1}{|\mathcal{K}|}\sum_{k\in\mathcal{K}} \frac{1}{N_s^{(k)}}\sum_{j=1}^{N_s^{(k)}} \frac{\left|i_L^{(k)}(t_j; x) - \hat{\imath}_L^{(k)}(t_j)\right|}{\hat{\imath}_L^{(k)}(t_j)}, \tag{16}$$

where $|\mathcal{K}|$ is the cardinality of the set $\mathcal{K}$, $\hat{\imath}_L^{(k)}$ is the measured current in the k-th dataset, and $i_L^{(k)}$ is the current obtained by solving system (3) (sampling the solution with step T_s), with parameter vector x and input $v = \hat{v}^{(k)}$, with the values of n and g corresponding to the k-th dataset.

Both models 1 and 2 are fitted by solving the optimization problem through a genetic algorithm, using the MATLAB function *ga* with default options [39]. The training set $\mathcal{K}$ comprises datasets obtained with $n = 30$, $g = \{0.2, 0.6, 1\}$ mm, and $f = \{20, 50\}$ kHz. Specifically, for each combination of

TABLE I
OPTIMAL PARAMETERS

MODEL 1		MODEL 2	
parameter	value	parameter	value
R_s	$0.119\,\Omega$	R_s	$0.137\,\Omega$
R_p	$2.47\,\mathrm{k\Omega}$	R_p	$3.24\,\mathrm{k\Omega}$
α	$0.299\,\mathrm{mm}^{-1}$	α	$0.336\,\mathrm{mm}^{-1}$
$\xi_3^{(1)}$	7.67	$\xi_3^{(2)}$	9.29
$\xi_1^{(1)}$	1621	c_1	$1174\,\mathrm{mH}^{-1}\cdot\mathrm{mm}^{-1}$
$\xi_4^{(1)}$	$187\,\mathrm{A}\cdot\mathrm{m}^{-1}$	c_2	$235\,\mathrm{mH}^{-1}$
		c_3	$0.430\,\mathrm{nH}$
		c_4	$294\,\mathrm{A}\cdot\mathrm{mm}^{-1}$
		c_5	$66\,\mathrm{A}$

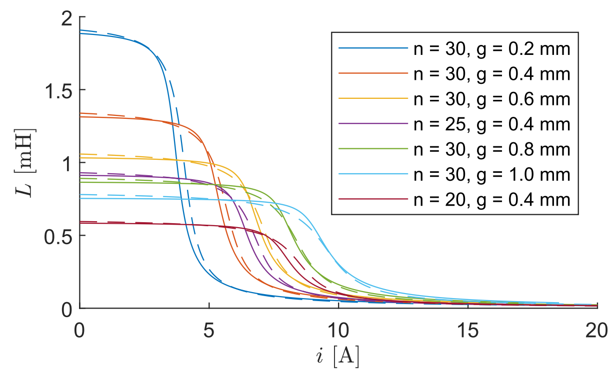

Fig. 9. Differential inductance L vs i for model 1 (continuous lines) and model 2 (dotted lines).

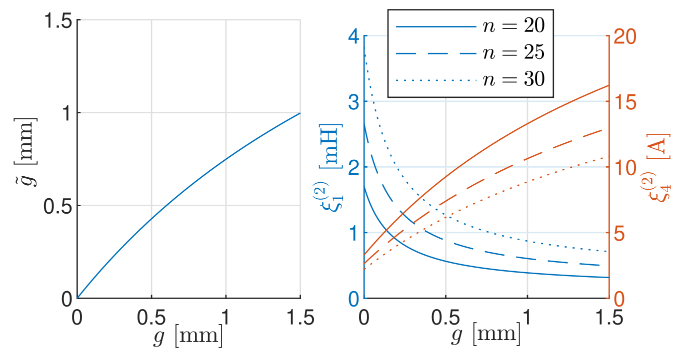

Fig. 10. Left panel: $\tilde{g}$ as a function of g; right panel: parameters $\xi_1^{(2)}$ and $\xi_4^{(2)}$ as function of g for three different values of n. These curves are obtained with model 2.

This article has been accepted for inclusion in a future issue of this journal. Content is final as presented, with the exception of pagination.

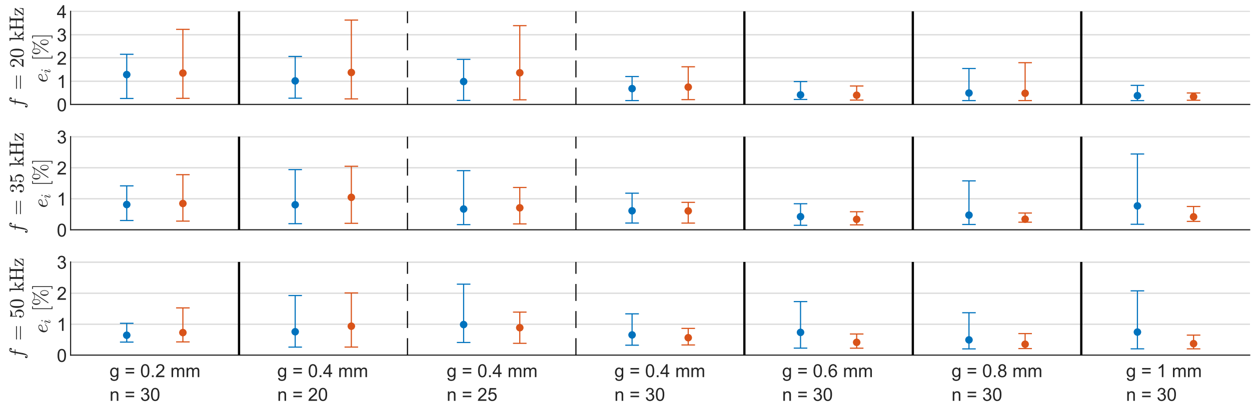

Fig. 11. Relative error e_i for all the datasets for model 1 (blue) and model 2 (orange). Mean (dot), maximum (upper bar), and minimum (lower bar) error across all amplitudes.

n, g, and f mentioned above, measurements with the smallest and largest current amplitudes, as well as two intermediate amplitudes, are included, resulting in $|\mathcal{K}| = 24$ datasets (out of 147 available) used to train the model. The resulting optimal parameters (vector x^*) are listed in Table I.

Fig. 9 shows the nonlinear inductance $L(i; n, g)$ obtained with model 1 (solid curves) and model 2 (dashed curves), for different values of n and g. As expected, as g increases or n decreases, the nominal inductance becomes smaller and the saturation occurs for higher current values. Notice that different combinations of n and g may lead to curves (e.g., the green and purple ones) with about the same nominal inductance but a different current range for the linear region. The difference between models 1 and 2 lies mainly in the shape of the function around the knee between the linear and nonlinear regions. The relationship between $\tilde{g}$ and g (see Eq. (6)) for model 2 is shown in the left panel of Fig. 10. Due to flux fringing, it appears that for a real gap of $g = 1$ mm, the effective gap reduces to about $\tilde{g} = 0.75$ mm. The right panel shows instead how parameters $\xi_1^{(2)}$ (left axis) and $\xi_4^{(2)}$ (right axis) vary with g, for different values of n. Notice that increasing the gap over a certain value does not affect $\xi_1^{(2)}$ significantly.

B. Model Validation

To validate the accuracy of the model, simulations are performed by integrating system (3) with $v = \hat{v}^{(k)}$, $\forall k$, i.e., the voltage measurements in all available datasets, with the optimal parameters. The resulting estimated current for the k-th dataset is $i_L^{(k)}(t_j; x^*)$, whereas the average power loss is $\langle p^{(k)} \rangle = \frac{1}{N_s^{(k)}} \sum_{j=1}^{N_s^{(k)}} \hat{v}^{(k)}(t_j) i_L^{(k)}(t_j; x^*)$. To measure the accuracy of the models we define the relative percent error on the current as

$$e_i^{(k)} = 100 \frac{1}{N_s^{(k)}} \sum_{j=1}^{N_s^{(k)}} \frac{\left| i_L^{(k)}(t_j; x^*) - \hat{\imath}_L^{(k)}(t_j) \right|}{\hat{\imath}_L^{(k)}(t_j)} \tag{17}$$

and the relative percent error on the power loss as

$$e_p^{(k)} = 100 \frac{\left| \langle p^{(k)} \rangle - \langle \hat{p}^{(k)} \rangle \right|}{\langle \hat{p}^{(k)} \rangle} \tag{18}$$

For each available value of n, g, and f, there are 7 datasets characterized by different current biases and amplitudes. Fig. 11 shows the minimum, maximum, and average errors e_i among these 7 datasets, for each triplet (n, g, f) and with model 1 (blue) and 2 (orange). The average error is represented by dots whereas the minimum and maximum values are the edges of the vertical segments. The two proposed models exhibit comparable accuracy, with model 2 performing slightly better than model 1. The mean and maximum current errors are always below 1.4% and 3.7%, respectively. We recall that measurements obtained with $n = \{20, 25\}$, $g = \{0.4, 0.8\}$ mm, and $f = 35$ kHz have not been used for model training, which testifies the good generalization capability of the models.

The minimum, maximum, and average errors e_p are shown in Fig. 12 (same kind of plots as in Fig. 11). Again, the two models exhibit similar performances. The mean error is always below 15%, whereas the maximum error exceeds 15% only for $g = 0.2$ mm and $f = 20$ kHz. In the worst case, however, the measured and estimated average powers are 6.01 W and 4.24 W, leading to an absolute error of 1.77 W.

Fig. 13 shows the measured (and filtered) and estimated (with model 2) currents for some operating conditions; the related errors e_i and e_p are reported in each panel (black for model 2, gray for model 1). Panels (a)-(c) show currents obtained with the inductor operating in its linear region, whereas panels (d)-(i) are related to a partially saturating behavior. Panels (h) and (i) correspond to the operating conditions with the worst error e_i and e_p, respectively. Notice the good match between estimations and measurements in almost all conditions. The results obtained with model 1 (omitted for brevity) are very similar, as also evidenced by similar error values.

C. Application of the Model to SMPS Design

Proposing an optimization algorithm for the optimal design of power converters exploiting partially saturating inductors is out of the scope of this paper. However, we want to show through an example how the proposed model can be an effective tool to accomplish this task. To this aim, we implemented the buck converter shown in Fig. 1 in Simulink, by exploiting the Simscape Electrical library, where the inductor is modeled through the circuit shown in Fig. 6,

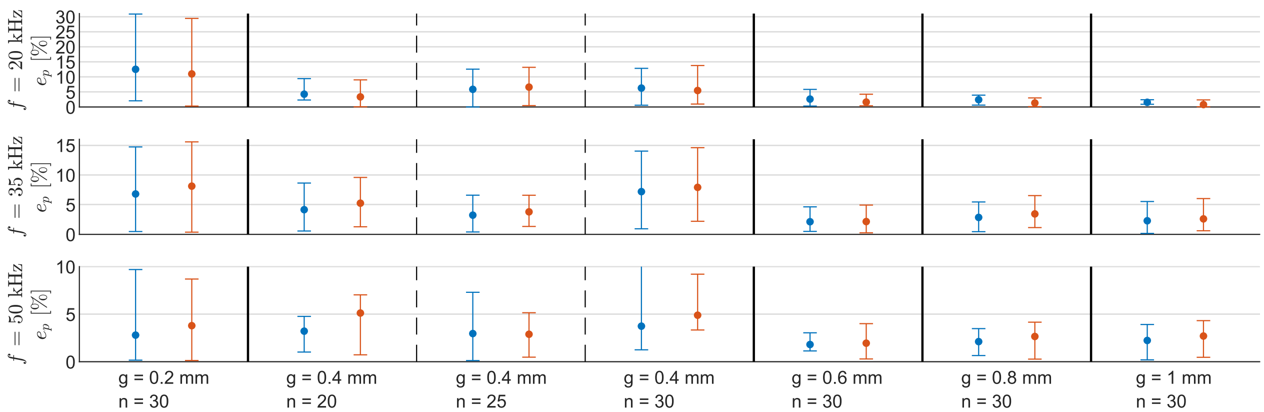

Fig. 12. Relative error e_p for all the datasets for model 1 (blue) and model 2 (orange). Mean (circle), maximum (upper bar), and minimum (lower bar) error across all amplitudes.

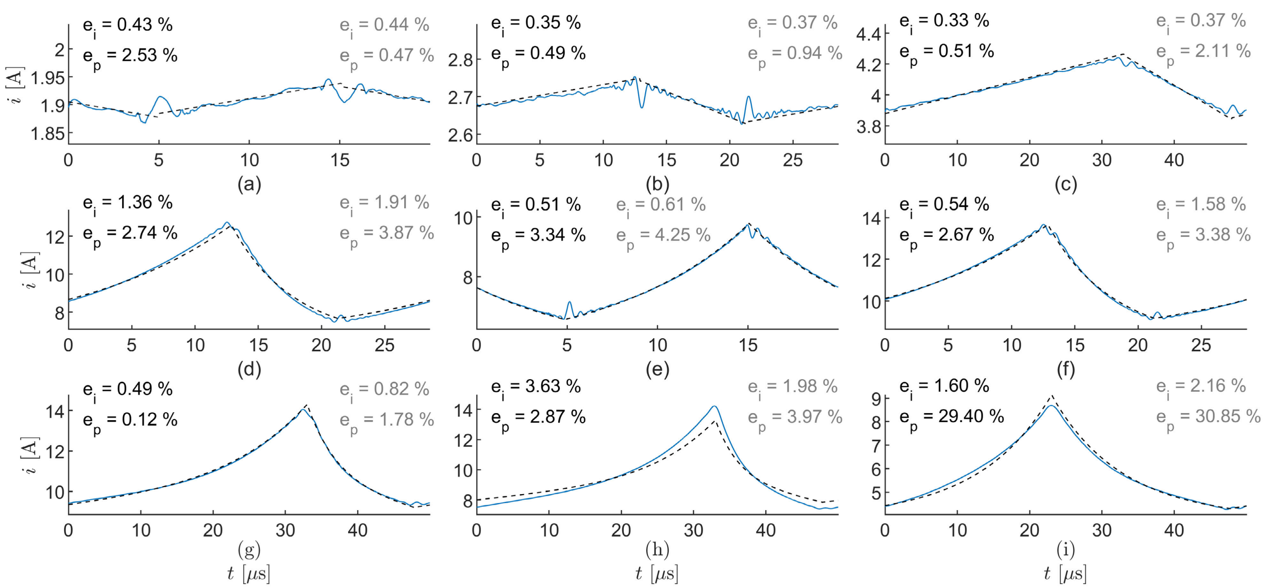

Fig. 13. Measured (blue curves) and estimated (black dashed curves) currents (with model 2) in 9 different operating conditions. The triplet (n, g, f) for each panel is: (a) (30, 0.2 mm, 50 kHz), (b) (30, 0.6 mm, 35 kHz), (c) (30, 1 mm, 20 kHz), (d) (25, 0.4 mm, 35 kHz), (e) (30, 0.4 mm, 50 kHz), (f) (30, 0.8 mm, 35 kHz), (g) (30, 1 mm, 20 kHz), (h) (20, 0.4 mm, 20 kHz), (i) (30, 0.2 mm, 20 kHz).

with model 1. We set the following operating conditions: $v_{in} = 100$ V, $D = 0.4$, $R = 5\,\Omega$, $f = 35$ kHz. The converter's average output voltage and power are about 40 V and 320 W, respectively, whereas the average inductor current is 8 A. We performed different simulations by changing the values of n and g and, for each of them, we computed the current ripple Δi at steady-state, as shown in Fig. 14. For each curve, when the gap exceeds a given value, the inductor always operates in its linear region and, as expected, the ripple - which is inversely proportional to the inductance - grows monotonically with g. For lower gap values, the inductor operates in partial saturation, and the ripple decreases until reaching a minimum value. By assuming that the design specifications impose a ripple lower than 30% of the average inductor current (about 2.4 A, see the black dashed line in the figure), it appears that all combinations of n and g leading to curve points below the black line are feasible design choices. We now focus on points A and B, such that Δi is 20% of the average inductor current, obtained with the lowest n and $g = 0.36$ mm and 0.73 mm, respectively. The corresponding inductor currents are the blue (point A) and orange (point B) curves in the left

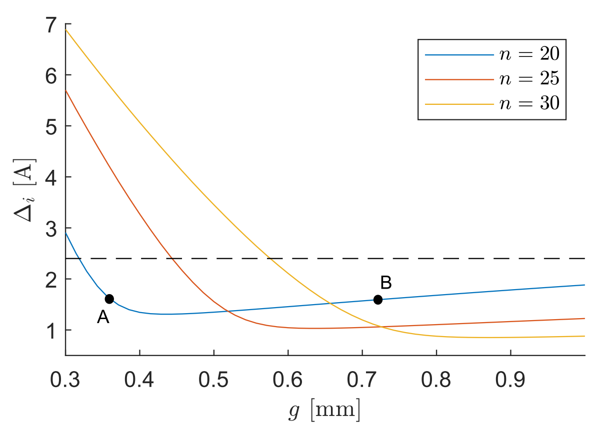

Fig. 14. Current ripple Δi as a function of g, for different values of n. The black dashed line marks the ripple threshold.

panel of Fig. 15. The right panel shows the related inductance $L(i; n, g)$ (thin lines) and the portion of the curve spanned by the current (thick lines). The same ripple can be obtained with the inductor either partially saturating (point A) or fully in its linear region (point B). The average power estimated by

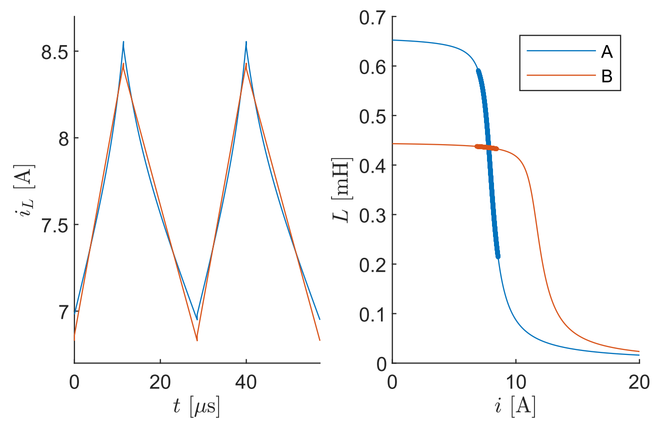

Fig. 15. Steady-state current i_L (left panel) and inductance L under operating conditions A (blue curves) and B (orange curves).

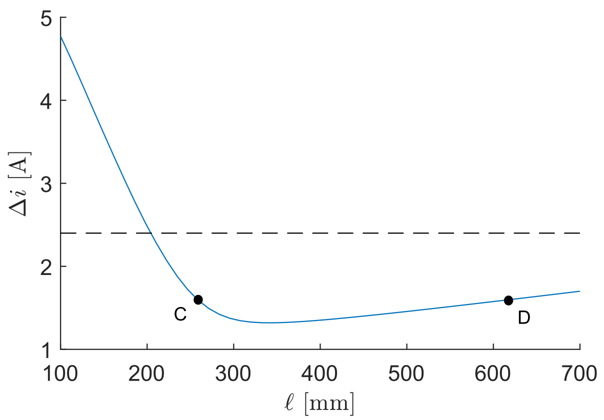

Fig. 16. Current ripple Δi as a function of ℓ. The black dashed line is the ripple threshold.

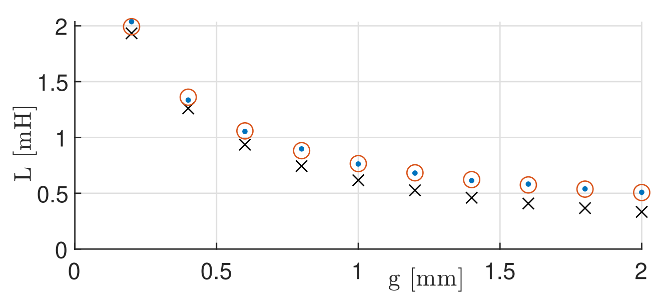

Fig. 17. Inductance $\hat{L}$ based on measurements (blue dots), values of L estimated by applying Eq. (7) (orange circles), and values of L estimated by applying Eq. (7) with $\alpha = 0$ (black crosses).

the model is about 8.11 W, in both points A and B, namely about 2.53% of the converter output power.

By fixing $n = 20$ and $g = 0.4$ mm and by varying the magnetic path ℓ between 300 mm and 800 mm, a similar ripple behavior is obtained, shown in Fig. 16. This behavior can be better understood by looking at Eqs. (10) and (11), where it appears that increasing g or ℓ has qualitatively the same effect. The proposed model has not been validated on data for different values of A and ℓ, therefore, Fig. 16 has only a qualitative meaning. Also in this case, both points C and D are feasible design choices. Here point C corresponds to an inductor with a magnetic path ℓ 2.4 times shorter than for point D. This means that if the saturating inductor is used, the converter's power density is increased. The section area A could be considered as a further design parameter.

Even if this analysis is only partial, as many other effects should be considered (i.e., the dependence of the working temperature on the core size, the switching and conduction losses of the semiconductor devices, and other converter operating conditions), it provides an insight into the potentialities of the proposed model from a design perspective.

V. Conclusion

In custom-made ferrite-core inductors, tuning the number of turns and the air-gap length allows for shaping the behavior of the inductance versus current. In this work, two behavioral inductor circuit models are obtained, in which the inductance depends on current, air-gap length, and number of turns. The models have been identified and validated by resorting to measurements on a real buck converter and proved to be accurate for different air-gap values, number of turns, and SMPS operating conditions. Model 1, based on physics, relies on 6 parameters and assumes that the core area and length are known. This model, once properly validated, possibly allows also including the core area and magnetic path length as design parameters. Model 2, fully black-box, needs 3 more parameters but achieves slightly better accuracy and does not require *a priori* knowledge.

Exploiting inductors in partial saturation allows increasing the power density of switching converters. In this framework, the proposed models can be embedded into a circuit simulator to mimic the behavior of a power converter, also when the inductor approaches magnetic saturation, for different values of air gap length and number of turns. This is particularly useful to optimally design custom inductors, by selecting the proper gap length and number of turns, to meet the converters' specifications. The model can even be used within optimization tools for optimal converter design, in the presence of inductors working in their nonlinear region. Moreover, the model-based control (such as model predictive control [40], [41]) of switching converters including inductors working in partial saturation needs behavioral models like the one proposed in this paper.

Appendix A
Experimental Validation of Eq. (6)

To validate Eq. (6), we performed some additional measurements by applying (directly to the inductor terminals) small-amplitude sinusoidal voltages at 20 kHz, so that the component works in its linear region. We kept $n = 30$ turns and changed the air gap length g from 0.2 to 2 mm. Based on the applied inductor voltage $v(t) = V cos(\omega t + \phi_v)$ and corresponding current $i_L(t) = I cos(\omega t + \phi_i)$, we estimated its impedance as $Z(j\omega) = \hat{R} + j\omega\hat{L} \triangleq \frac{V}{I} e^{j(\phi_v - \phi_i)}$, thus obtaining the inductance $\hat{L}$. We computed L through Eq. (7), by fitting parameters μ_d and α to $\hat{L}$. The optimal parameter values for this experimental setting turn out to be $\mu_d = 1750$ and $\alpha = 294\,\mathrm{m}^{-1}$. Fig. 10 shows $\hat{L}$ (from measurements) as blue dots and L (from Eq. (7)) as orange circles. If the fringing effect is not considered ($\alpha = 0$), Eq. (7) provides the inductance values shown as black crosses, which are less and less accurate as g increases. The above values of μ_d and α are slightly different from the ones listed in Tab. I, which have been obtained based on all measurements with different input waveforms, number of turns, and frequencies. The good matching between $\hat{L}$ and L confirms that the model correctly accounts for the fringing effect.

Appendix B
Derivation of the Parameters of Model 2

We recall that, for model 2, $L(i; n, g) \approxeq \xi_1^{(2)}$ for $i \to 0$. Starting from Eq. (11), for $H \to 0$ (then, $i \to 0$), $\mu_d \approxeq \xi_1^{(1)}$; then,

$$\xi_1^{(2)}(n, g) = \frac{n^2 A \mu_0 \xi_1^{(1)}}{\ell + \tilde{g}\xi_1^{(1)}} = \frac{n^2}{c_1 \tilde{g} + c_2} \tag{19}$$

with $c_1 \triangleq \frac{\xi_1^{(1)}}{A\mu_0\xi_1^{(1)}}$ and $c_2 \triangleq \frac{\ell}{A\mu_0\xi_1^{(1)}}$. On the contrary, $L(i; n, g) \approxeq \xi_2^{(2)}$ for large values of i. If H (and then i) are large, $\mu_d \approxeq 1$, then

$$\xi_2^{(2)}(n) = \frac{n^2 A \mu_0}{\ell + \tilde{g}} \approxeq \frac{n^2 A \mu_0}{\ell} = n^2 c_3 \tag{20}$$

since $\ell \gg g$, with $c_3 \triangleq \frac{\mu_0 A}{\ell}$.

Term $\xi_4^{(2)}$ is the current value such that $L\left(\xi_4^{(2)}; n, g\right) = \bar{L}(n, g) = 0.5\left(\xi_1^{(2)}(n, g) + \xi_2^{(2)}(n)\right) \approxeq 0.5\xi_1^{(2)}(n, g)$, since $\ell \gg g$ and $\xi_1^{(1)} \gg 1$. The inductance $\bar{L}(n, g)$ is obtained for $\mu_d = \bar{\mu}_d(g)$, which can be derived by substituting $\bar{L}(n, g)$ in the left-hand-side of Eq. (10):

$$\bar{\mu}_d(g) = \frac{0.5\xi_1^{(1)}\ell}{\ell + 0.5\xi_1^{(1)}\tilde{g}}. \tag{21}$$

It appears that if $g = 0$ then $\bar{L}(n, g)$ corresponds exactly to the mid value of the permeability $\left(\bar{\mu}_d = 0.5\xi_1^{(1)}\right)$, obtained for $\bar{H} = \bar{H}_0$ and $\bar{B} = \bar{B}_0$ (see Fig. 8, top panels). As g increases, $\bar{\mu}_d$ decreases, leading to an increment of both $\bar{H}$ and $\bar{B}$. For sufficiently small values of g, $\bar{\mu}_d$ remains in the high-slope part of the $\mu_d(H)$ curve in panel (a), which implies small deviations of $\bar{H}$ and even smaller deviations of $\bar{B}$, that approaches saturation. Then we can write $\bar{H} = \left(1 + a\frac{\tilde{g}}{G}\right)\bar{H}_0$ and $\bar{B} = (1 + b\frac{\tilde{g}}{G})\bar{B}_0$, with $a, b \ll 1$ and G is the maximum considered gap, so that $\frac{g}{G} < 1$. By substituting these terms in Eq. (10), we obtain $\xi_4^{(2)}(n, g)$, i.e., the value of the current that brings to $\bar{L}(n, g)$:

$$\xi_4^{(2)}(n, g) = \frac{1}{n}\left[\left(1 + a\frac{\tilde{g}}{G}\right)\bar{H}_0\ell + \left(1 + b\frac{\tilde{g}}{G}\right)\frac{\bar{B}_0 G}{\mu_0}\frac{\tilde{g}}{G}\right] \tag{22}$$

$$= \frac{1}{n}\left[\frac{b\bar{B}_0 G}{\mu_0}\left(\frac{\tilde{g}}{G}\right)^2 + \left(\frac{a\bar{H}_0\ell}{G} + \frac{\bar{B}_0 G}{\mu_0}\right)\frac{\tilde{g}}{G} + \bar{H}_0\ell\right] \tag{23}$$

which is a quadratic function of $\tilde{g}$. Since $\frac{\tilde{g}}{G} < 1$ and the coefficient of the quadratic term is much smaller than the coefficient of the linear term ($b \ll 1$), we can consider

$$\xi_4^{(2)}(n, g) = \frac{c_4\tilde{g} + c_5}{n} \tag{24}$$

with $c_4 \triangleq \frac{a\bar{H}_0\ell}{G^2} + \frac{\bar{B}_0}{\mu_0}$ and $c_5 \triangleq \bar{H}_0\ell$.

References

[1] W. G. Hurley and W. H. Wlfle, *Transformers and Inductors for Power Electronics: Theory, Design and Applications*. Hoboken, NJ, USA: Wiley, 2013.

[2] R. Hilzinger and W. Rodewald, *Magnetic Materials: Fundamentals, Products, Properties, and Applications*. Hanau, Germany: Vacuumschmelze, 2013.

[3] E. C. Snelling, *Soft Ferrites: Properties and Applications*. Scotland, U.K.: Iliffe Books Ltd, 1969.

[4] R. A. Salas and J. Pleite, "Simulation of the saturation and air-gap effects in a POT ferrite core with a 2-D finite element model," *IEEE Trans. Magn.*, vol. 47, no. 10, pp. 4135–4138, Oct. 2011.

[5] R. S. Kasikowski and B. Wiecek, "Fringing-effect losses in inductors by thermal modeling and thermographic measurements," *IEEE Trans. Power Electron.*, vol. 36, no. 9, pp. 9772–9786, Sep. 2021.

[6] R. Jez, "Influence of the distributed air gap on the parameters of an industrial inductor," *IEEE Trans. Magn.*, vol. 53, no. 11, pp. 1–5, Nov. 2017.

[7] P. Winkler and W. Guenther, "Using powder materials to replace air-gaps for fringing flux reduction," in *Proc. PCIM Eur., Int. Exhibition Conf. Power Electron., Intell. Motion, Renew. Energy Energy Manage.*, May 2017, pp. 1–6.

[8] L. Milner and G. A. Rincón-Mora, "Small saturating inductors for more compact switching power supplies," *IEEJ Trans. Electr. Electron. Eng.*, vol. 7, no. 1, pp. 69–73, Jan. 2012.

[9] G. Di Capua, N. Femia, and K. Stoyka, "Switching power supplies with ferrite inductors in sustainable saturation operation," *Int. J. Electr. Power Energy Syst.*, vol. 93, pp. 494–505, Dec. 2017.

[10] N. Femia, K. Stoyka, and G. D. Capua, "Impact of inductors saturation on peak-current mode control operation," *IEEE Trans. Power Electron.*, vol. 35, no. 10, pp. 10969–10981, Oct. 2020.

[11] M. S. Perdigão, J. P. F. Trovão, J. M. Alonso, and E. S. Saraiva, "Large-signal characterization of power inductors in EV bidirectional DC–DC converters focused on core size optimization," *IEEE Trans. Ind. Electron.*, vol. 62, no. 5, pp. 3042–3051, May 2015.

[12] Z. Yao et al., "Nonlinear inductor-based single sensor current balancing method for interleaved DC–DC converters," *IEEE Trans. Power Electron.*, vol. 39, no. 4, pp. 3996–4000, Apr. 2024.

[13] C. Ragusa et al., "Computation of current waveform in ferrite power inductors for application in buck-type converters," *J. Magn. Magn. Mater.*, vol. 502, May 2020, Art. no. 166458.

[14] D. Scirè, G. Vitale, M. Ventimiglia, and G. Lullo, "Non-linear inductors characterization in real operating conditions for power density optimization in SMPS," *Energies*, vol. 14, no. 13, p. 3924, Jun. 2021.

[15] W. Yuan, Y. Wang, D. Liu, F. Deng, and Z. Chen, "Impacts of inductor nonlinear characteristic in multiconverter microgrids: Modeling, analysis, and mitigation," *IEEE J. Emerg. Sel. Topics Power Electron.*, vol. 8, no. 4, pp. 3333–3347, Dec. 2020.

[16] Z. Özkan and A. M. Hava, "Current control of single-phase VSC systems with inductor saturation using inverse dynamic model-based compensation," *IEEE Trans. Ind. Electron.*, vol. 66, no. 12, pp. 9268–9277, Dec. 2019.

[17] Z. Özkan and A. M. Hava, "Inductor saturation compensation in three-phase three-wire voltage-source converters via inverse system dynamics," *IEEE Trans. Ind. Electron.*, vol. 69, no. 5, pp. 4309–4319, May 2022.

[18] Y. Gao, Y. Tang, H. Sun, Y. Guo, G. Liu, and H. Yang, "Variable saturation inductor-based full bridge converter with wide ZVS range and reduced duty cycle loss," *IEEE Trans. Ind. Electron.*, vol. 69, no. 11, pp. 11055–11066, Nov. 2022.

[19] J. Kaiser and T. Dürbaum, "An overview of saturable inductors: Applications to power supplies," *IEEE Trans. Power Electron.*, vol. 36, no. 9, pp. 10766–10775, Sep. 2021.

[20] M. Akbari, A. Rezaei-Zare, M. A. M. Cheema, and T. Kalicki, "Air gap inductance calculation for transformer transient model," *IEEE Trans. Power Del.*, vol. 36, no. 1, pp. 492–494, Feb. 2021.

[21] E. Stenglein and M. Albach, "Analytical calculation method for the non-linear characteristic of ferrite-cored inductors with stepped air gap," *Electr. Eng.*, vol. 99, no. 1, pp. 421–429, Mar. 2017.

[22] A. Oliveri, M. Lodi, and M. Storace, "Nonlinear models of power inductors: A survey," *Int. J. Circuit Theory Appl.*, vol. 50, no. 1, pp. 2–34, Jan. 2022.

[23] K. Stoyka, N. Femia, and G. Di Capua, "Power inductors behavioral modeling revisited," *IEEE Trans. Circuits Syst. I, Reg. Papers*, vol. 67, no. 12, pp. 5636–5649, Dec. 2020.

[24] D. Scirè, G. Lullo, and G. Vitale, "Non-linear inductor models comparison for switched-mode power supplies applications," *Electronics*, vol. 11, no. 15, p. 2472, Aug. 2022.

[25] G. Vitale, G. Lullo, and D. Scirè, "Thermal stability of a DC/DC converter with inductor in partial saturation," *IEEE Trans. Ind. Electron.*, vol. 68, no. 9, pp. 7985–7995, Sep. 2021.

[26] A. Ravera, A. Oliveri, M. Lodi, and M. Storace, "A nonlinear behavioral model of a ferrite-core inductor with fixed-frequency sinusoidal voltage input," in *Proc. IEEE 20th Int. Conf. Smart Technol.*, Jul. 2023, pp. 418–422.

[27] A. Oliveri, M. Lodi, C. Beatrice, E. Ferrara, M. Storace, and F. Fiorillo, "Behavioral model of an amorphous-core inductor working up to partial saturation," in *Proc. IEEE Int. Symp. Circuits Syst. (ISCAS)*, May 2022, pp. 1522–1526.

[28] M. Lodi, F. Bizzarri, D. Linaro, A. Oliveri, A. Brambilla, and M. Storace, "A nonlinear behavioral ferrite-core inductance model able to reproduce thermal transients in switch-mode power supplies," *IEEE Trans. Circuits Syst. I, Reg. Papers*, vol. 67, no. 4, pp. 1255–1263, Apr. 2020.

[29] A. Oliveri, G. Di Capua, K. Stoyka, M. Lodi, M. Storace, and N. Femia, "A power-loss-dependent inductance model for ferrite-core power inductors in switch-mode power supplies," *IEEE Trans. Circuits Syst. I, Reg. Papers*, vol. 66, no. 6, pp. 2394–2402, Jun. 2019.

[30] M. Lodi, A. Oliveri, and M. Storace, "Pareto-optimal selection of saturating inductors in the design of switch-mode power supplies," in *Proc. 21st Eur. Conf. Power Electron. Appl.*, Sep. 2019, pp. P1–P9.

[31] K. Stoyka, G. Di Capua, and N. Femia, "Normalized inductance modeling for ferrite power inductor families," in *Proc. 26th IEEE Int. Conf. Electron., Circuits Syst.*, Nov. 2019, pp. 843–846.

[32] A. Ravera, A. Formentini, M. Lodi, A. Oliveri, and M. Storace, "A nonlinear model of air-gapped ferrite-core inductors for SMPS applications," in *Proc. IEEE Int. Symp. Circuits Syst. (ISCAS)*, May 2024, pp. 1–19.

[33] L. Chua, "Device modeling via nonlinear circuit elements," *IEEE Trans. Circuits Syst.*, vols. CS-27, no. 11, pp. 1014–1044, Nov. 1980.

[34] Magn. *Ferrite Cores Catalog*. Accessed: Nov. 10, 2023. [Online]. Available: https://www.mag-Inc.com/Media/Magnetics/File-Library/Product%20Literature/Ferrite%20Literature/Magnetics-2021-Ferrite-Catalog.pdf

[35] F. Fiorillo, *Characterization and Measurement of Magnetic Materials*. San Diego, CA, USA: Academic Press, 2004.

[36] Z. H. Khan, M. M. Rahman, S. S. Sikder, M. A. Hakim, and D. K. Saha, "Complex permeability of Fe-deficient Ni–Cu–Zn ferrites," *J. Alloys Compounds*, vol. 548, pp. 208–215, Aug. 2013.

[37] W. G. Hurley and W. H. Wölfle, *Transformers and Inductors for Power Electronics: Theory, Design and Applications*. Hoboken, NJ, USA: Wiley, 2013.

[38] G. Di Capua and N. Femia, "A novel method to predict the real operation of ferrite inductors with moderate saturation in switching power supply applications," *IEEE Trans. Power Electron.*, vol. 31, no. 3, pp. 2456–2464, Mar. 2016.

[39] MathWorks, *Global Optimization Toolbox User's Guide*. Natick, MA, USA: The MathWorks, Inc., 2023, ch. 8.

[40] P. Karamanakos, E. Liegmann, T. Geyer, and R. Kennel, "Model predictive control of power electronic systems: Methods, results, and challenges," *IEEE Open J. Ind. Appl.*, vol. 1, pp. 95–114, Aug. 2020. [Online]. Available: https://ieeexplore.ieee.org/abstract/document/9180048

[41] D. Wang et al., "Model predictive control using artificial neural network for power converters," *IEEE Trans. Ind. Electron.*, vol. 69, no. 4, pp. 3689–3699, Apr. 2022.

Alessandro Ravera (Student Member, IEEE) received the B.Sc. degree in electronic engineering and information technology and the M.Sc. degree in electronic engineering from the University of Genoa, Italy, in 2019 and 2021, respectively, where he is currently pursuing the Ph.D. degree. His current research interests include the modeling of nonlinear systems and the design and implementation of digital embedded systems.

Andrea Formentini (Member, IEEE) received the M.S. degree in computer engineering and the Ph.D. degree in electrical engineering from the University of Genoa, Genoa, in 2010 and 2014, respectively. He then started working as a Research Fellow with the Power Electronics, Machines and Control Group, University of Nottingham. In September 2018, he became an Assistant Professor with the University of Nottingham. In 2021, he joined the University of Oxford as a Lecturer of engineering science. He is currently an Associate Professor with the University of Genoa, where he pursues research in control of power electronics and electric drives.

Matteo Lodi (Member, IEEE) received the Laurea (M.Sc.) and Ph.D. degrees in electrical engineering from the University of Genoa, Italy, in 2015 and 2019, respectively. He currently holds a post-doctoral position with the Department of Electrical, Electronic, Telecommunications Engineering, and Naval Architecture, University of Genoa. His research interests include the modeling of nonlinear systems, bifurcation analysis, and nonlinear dynamics.

Alberto Oliveri (Member, IEEE) received the M.Sc. and Ph.D. degrees in electronic engineering and electrical engineering from the University of Genoa (UNIGE), Italy, in 2009 and 2013, respectively. He is currently an Associate Professor with the Department of Electrical, Electronic, Telecommunications Engineering, and Naval Architecture, UNIGE. His main research interests include nonlinear modeling (applied to power electronics, power grids, and soft robotics) and predictive control.

Massimiliano Passalacqua (Member, IEEE) was born in Genoa, Italy, in 1993. He received the B.S. (Hons.), M.S. (Hons.), and Ph.D. degrees in electrical engineering from the University of Genoa, in 2015, 2017, and 2021, respectively. He is currently a Research Fellow with the Department of Electrical, Electronic and Telecommunication Engineering and Naval Architecture (DITEN), University of Genoa. His research interests include power electronics, control for electrical drives, and hybrid electric vehicles.

Marco Storace (Senior Member, IEEE) was born in Genoa, Italy, in 1969. He received the Laurea (M.Sc.) degree (summa cum laude) in electronic engineering and the Ph.D. degree in electrical engineering from the University of Genoa in March 1994 and April 1998, respectively. Since 2011, he has been a Full Professor with the University of Genoa. He was a Visitor with EPFL, Lausanne, Switzerland, in 1998 and 2002. He has authored or co-authored about 180 scientific articles, more than an half of which have been published in international journals. He has co-authored *Linear and Nonlinear Circuits: Basic and Advanced Concepts* (two volumes). His current research interests include nonlinear circuit theory and applications, analysis and modeling of nonlinear dynamical systems, and networked. He is a member of the IEEE Technical Committee on Nonlinear Circuits and Systems (TC-NCAS). He served as the Chair for the Nonlinear Circuits and Systems Technical Committee from 2021 to 2023 and an Associate Editor for IEEE TRANSACTIONS ON CIRCUITS AND SYSTEMS—II: EXPRESS BRIEFS from 2008 to 2009.

Open Access funding provided by 'Università degli Studi di Genova' within the CRUI CARE Agreement